J Nanopart Res (2015) 17:339
DOI 10.1007/s11051-015-3131-1

RESEARCH PAPER

Facile synthesis of $MgCo_2O_4$ nanowires as binder-free flexible anode materials for high-performance Li-ion batteries

Xiujuan Wang · Gaohong Zhai · Hui Wang

Received: 4 March 2015 / Accepted: 23 July 2015 / Published online: 14 August 2015

Abstract $MgCo_2O_4$ nanowires are synthesized for the first time through two-step synthesis method, followed by annealing of the $MgCo_2O_4$ precursors. The microstructure and morphology of $MgCo_2O_4$ nanowires are examined by powder X-ray diffraction, scanning electron microscopy, high-resolution transmission electron microscopy, and X-ray photoelectron spectroscopy. $MgCo_2O_4$ nanowires give rise to a BET surface area of 45.1 $m^2\ g^{-1}$ and the adsorption average pore size of 11.5 nm. When tested as an anode for lithium-ion batteries, the $MgCo_2O_4$ nanowires electrode exhibit exceptional properties in terms of specific capacity, cycling performance, and rate capacity compared with previously reported Co-based binary metal oxides. For instance, when the current densities increase from 5, 10, 15, and 20 A g^{-1}, the discharge capacities of the $MgCo_2O_4$ nanowires electrode are about 649, 348, 188, and 121 mAh g^{-1}, respectively. The enhanced electrochemical performance of the $MgCo_2O_4$ nanowires can be mainly attributed to the nanostructures which lead to decreased lithium-ion diffusion distances and increased active sites for Li insertion/extraction reactions.

Keywords $MgCo_2O_4$ · Nanostructures · Binder-free · Anode · Lithium-ion battery · Energy conversion

X. Wang · G. Zhai (✉) · H. Wang (✉)
Key Laboratory of Synthetic and Natural Functional Molecule Chemistry (Ministry of Education), College of Chemistry & Materials Science, Northwest University, Xi'an 710069, People's Republic of China
e-mail: zgh@nwu.edu.cn

H. Wang
e-mail: hwangnwu@sina.cn; huiwang@nwu.edu.cn

Introduction

The depletable traditional energy resources and the increasing urgent attentions to environmental pollution are main driving forces for the development of renewable and clean energy sources (Mondal et al. 2014; Tian et al. 2007). As one of the most promising type of energy storage device, lithium-ion batteries (LIBs) have attracted more and more attention in recent years due to its high-power capability, long cycle lifetime, and fast charge and discharge rates, such as mobile communication devices, portable electronics stationary, and energy storage. (Lou et al. 2014; Zhao et al. 2012; Cherian et al. 2013). It is well known that the capacity of anode material for lithium storage relates to their morphology and microstructure. The precise design of materials with controlled nanosized shapes provides one of the most effective ways of developing high-performance energy devices, because the high surface area of nanostructures leads to decreased lithium-ion diffusion distances and increased active sites for Li insertion/extraction reactions (Bai et al. 2014; Wang et al. 2011; Fu et al. 2013).

Recently, various nanostructured transition-metal oxides (TMO) have been exploited as one of the most promising candidates for potential application in energy-related devices, owing to their higher theoretical reversible capacities. (e.g., 782 mAh g^{-1} of SnO_2 (Li et al. 2010); 717 mAh g^{-1} of NiO (Aravindan et al. 2013); and 890 mAh g^{-1} of Co_3O_4 (Xiao et al. 2013). Among the TMO, cobalt-based nanomaterials have shown the highest capacity and the best electrochemical performances, compared to nickel oxide and iron oxides. (Du et al. 2011). However, cobalt is toxic and expensive, numerous efforts are made toward replacing Co_3O_4 partially with other inexpensive and environmentally friendly metal oxides to lower the toxicity and reduce the cost (Sharma et al. 2007a; Mondal et al. 2014). To date, many binary metal oxides, such as $CuCo_2O_4$ (Sharma et al. 2007b), $ZnCo_2O_4$ (Luo et al. 2012), $FeCo_2O_4$, $MgCo_2O_4$ (Sharma et al. 2008), $MnCo_2O_4$ (Li et al. 2014a), and $NiCo_2O_4$ (Shen et al. 2014), have also been reported as preliminary anode materials for LIBs. Among them, although $NiCo_2O_4$ and $FeCo_2O_4$ exhibit higher theoretical reversible capacities (890 and 900 mAh g^{-1}, respectively), the simple structures, poor electric conductivity, and severe volume variations during the electrochemical reaction led to structural instabilities and fast capacity decrease, especially. They show poor rate capability which is the most important for practical applications of LIBs. Mohamed et al. reported $FeCo_2O_4$ nanoflakes, the reversible capacity is $\sim$1570 mAh g^{-1} at a current density of 0.2 A g^{-1}, then $\sim$1433 mAh g^{-1} at 0.4 A g^{-1}, and $\sim$1222 mAh g^{-1} at 0.8 A g^{-1} (Mohamed et al. 2014). Li et al. synthesized $NiCo_2O_4$ microspheres, the discharge capacities of which are 753, 556, and 393 mA h g^{-1}, as the current density increased stepwise to 0.4, 0.8, and 1.6 A g^{-1}, respectively (Li et al. 2013). One strategy can be proposed to buffer the volume variations and improve the rate capability. It could use Co-based binary metal oxides like ACo_2O_4 during the first discharge, cobalt metal atoms are extruded from the pristine material, and a metal atoms form inactive metal oxides particles, which can inhibit the volume change (Chamas et al. 2013; Liu et al. 2014). Although $MgCo_2O_4$ shows the lower theoretical capacity ($\sim$780 mAh g^{-1}) compared with $FeCo_2O_4$ and $NiCo_2O_4$, during the first discharge, Mg atoms form inactive MgO. The inactive MgO can remit volume variations effectively during the electrochemical reaction. There are only a few reports on the application of $MgCo_2O_4$ as an anode material. Chowdari et al. first reported the preparation of needle-shape $MgCo_2O_4$ as an anode material for LIBs, the obtained $MgCo_2O_4$ showed electrochemical performances with an initial reversible capacity of 900 mAh g^{-1} and 17 % of the capacity (160 mAh g^{-1}) was retained over 50 cycles at a current of 60 mA g^{-1}(Sharma et al. 2008). However, the needle-shape $MgCo_2O_4$ showed low reversible capacity and poor cycling performance in practical application. Therefore, it is necessary to further improve the capacity, cyclic stability, and rate performance of $MgCo_2O_4$.

In this study, we report a simple and mild route at relatively low temperature (100 °C) to fabricate $MgCo_2O_4$ nanowires by two-step synthesis method. What's more, there is still no report in the literature to fabricate $MgCo_2O_4$ nanowires on Ni foam as binder-free electrodes. $MgCo_2O_4$ nanowires connected directly with Ni foam can provide numerous efficient transport pathways for ions and electrons and avoid the use of polymer binders and conducting additives. When applied as anode materials for LIBs, the $MgCo_2O_4$ nanowires exhibit remarkable rate performance and excellent cycling stability even at a high charge/discharge current density.

Experimental

Synthesis of $MgCo_2O_4$ nanowires on Ni foam

In a typical synthesis, 1 mmol $Mg(NO_3)_2{\cdot}6H_2O$, 2 mmol $Co(NO_3)_2{\cdot}6H_2O$, 12 mmol $CO(NH_2)_2$, and 6 mmol of hexamethylene-tetramine were dissolved in 30 ml distilled water and stirred for several minutes. After putting a Ni foam wafer (16 mm in diameter and 1 mm in thickness) treated with 3 M HCl solution for 30 min, the solution was then transferred into a 50 ml Teflon-lined stainless autoclave and maintained at 100 °C for 8 h. During the hydrothermal process, hydrolysis–precipitation took place, which produced the precipitated precursor of Mg, Co-hydroxide-carbonate on the Ni foam wafer (Kang et al. 2013). After hydrothermal growth, the resulting Mg, Co-hydroxide-carbonate was taken out and washed with distilled water and absolute ethanol for 10 times, and then dried at 60 °C for 12 h. Finally, the precursor was annealed

at a low temperature of 350 °C for 3 h to obtain $MgCo_2O_4$ nanowires. The representative synthetic process of the sample is illustrated in Fig. 1. For comparison, the powder product of $MgCo_2O_4$ was also produced by following the same procedure except that no Ni foam wafer was introduced.

Material characterization

Powder X-ray diffraction (XRD) patterns of samples were recorded by a Bruker D8 ADVANCE X-ray powder diffractometer using Cu K_α radiation ($\lambda = 0.15418$ nm) at a scanning rate of 0.02° s^{-1} in the 2θ range from 30 to 70°. Scanning electron microscopy (SEM) images of samples were carried out by a FEI Quanta 400 ESEM-FEG (environmental scanning electron microscope-field emission gun) equipped with an X-ray energy dispersive spectrometer (EDS). The microstructures of these nanowires were observed by transmission electron microscopy (TEM, FEI, Tecnai-20) and high-resolution transmission electron microscopy (HRTEM, J JEOL JEM-3010). The specific surface area and pore size distribution of the samples were recorded using nitrogen adsorption via Brunauer–Emmett–Teller (BET, TriStar 3020 analyzer) and Barrett–Joyner–Halenda (BJH) method at 77 K.

Electrochemical measurements

Electrochemical measurements were performed at 25 °C using coin cells (CR2025) with pure lithium foil as the counter and reference electrode. The $MgCo_2O_4$ microspheres electrode consisted of 80 % active material, 10 % of acetylene black, and 10 % of PVDF using *N*-methyl pyrrolidone (NMP) as solvent, and then the mixed suspension was pasted on Ni foam wafer (16 mm in diameter and 1 mm in thickness). After drying in a vacuum oven for 12 h at 80 °C, the nickel foam was pressed at 20 MPa so as to obtain good contact between nickel foam and the active material, the $MgCo_2O_4$ microsphere electrode was thus obtained. The $MgCo_2O_4$ nanowires grown on Ni foam wafer ($MgCo_2O_4$ loading: $\sim$2 mg cm^{-2}) sample were directly used as working electrode without any binders or conductive additives. Cells were constructed in a glove box in argon atmosphere under a dew point below −65°. The electrolyte was 1 M $LiPF_6$ dissolved in a mixture of dimethyl carbonate, diethyl carbonate, and ethylene carbonate (1:1:1 by volume), and the separator was microporous polypropylene film. The electrochemical experiments were carried out on a LAND battery program-control test system in cut-off voltages of 0.005 and 3.0 V. Cyclic voltammetry (CV) was carried out on a CHI 660D electrochemical workstation at a scan rate of 0.1 mV s^{-1} in the potential range of 0–3.0 V vs. Li/Li^+. Electrochemical impedance spectroscopy (EIS) was performed by using the same electrochemical workstation with the frequency range from 0.01 to 100 kHz.

Results and discussion

In order to study the crystal structure and phase purity of the obtained products, $MgCo_2O_4$ nanowires grown on Ni foam were sonicated for 1 h to peel the nanowires off from the substrate. As shown in Fig. 2, seven distinct diffraction peaks are observed at 2θ values of 31.03, 36.81, 38.27, 44.60, 55.19, 58.89, and 64.98°, respectively. All of these diffraction peaks can be indexed to (220), (311), (222), (400), (422), (511), and (440) crystal planes and assigned to $MgCo_2O_4$ with a spinel crystalline structure (JCPDS No. 02-1073). No additional diffraction peaks from

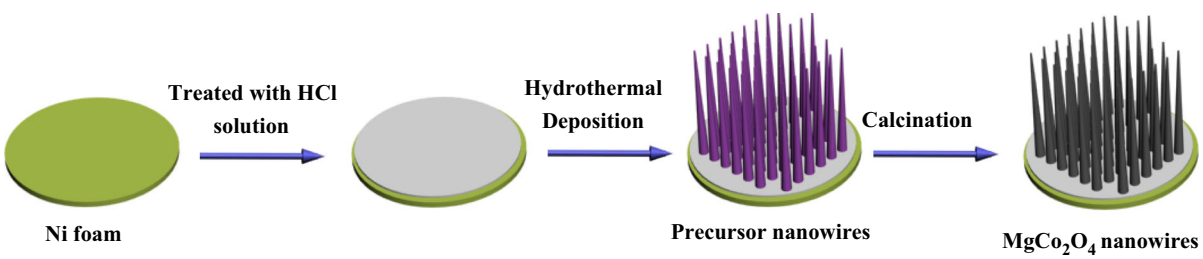

Fig. 1 Schematic mechanism of the fabrication process of $MgCo_2O_4$ nanowires

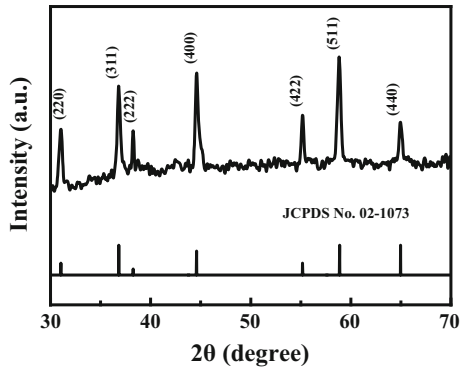

Fig. 2 X-ray diffraction patterns of $MgCo_2O_4$ nanowires

other than $MgCo_2O_4$ are detectable, indicating the high purity of the synthesized product.

The typical survey XPS spectrum of the product is depicted by using a Gaussian fitting method, the Co 2p emission spectrum (Fig. 3a) is best fitted with two spin-orbit doublets, characteristic of Co^{2+} and Co^{3+} (Xie et al. 2013). The peaks located at 51 eV in Fig. 3b reveal the high-resolution Mg 2p spectrum, and the results are in good agreement with the literature (Casey et al. 2008; Corneille et al. 1994). Figure 3c reveals the high-resolution O1 s spectrum; it comprises two oxygen contributions, the component O1 at 529.6 eV is typical of metal–oxygen bonds, another peak at 532.5 eV corresponds to a higher number of defect sites with low oxygen coordination usually observed in materials with small particles(Yuan et al. 2012).

The morphology of the as-synthesized $MgCo_2O_4$ nanowires is characterized by SEM, as shown in Fig. 4a–f. It can be clearly observed from Fig. 4a that the Ni foam is constructed by plenty of Ni belts with smooth surface. Figure 4b–d shows the gradually high-magnification SEM images of $MgCo_2O_4$ nanowires. It is observed that these $MgCo_2O_4$ nanowires are directly grown from and closely contacted with the Ni substrate. These nanowires have an edge length of 1–3 μm and a uniform thickness of ~60 nm. In comparison, without the Ni foam as the substrate, the formed $MgCo_2O_4$ nanowires are assembled in spherical shapes without uniform direction (Fig. 4e, f); this is because the nanowires unites often possess high surface free energy, and they tend to stack together and form sphere structure to minimize the total energy of

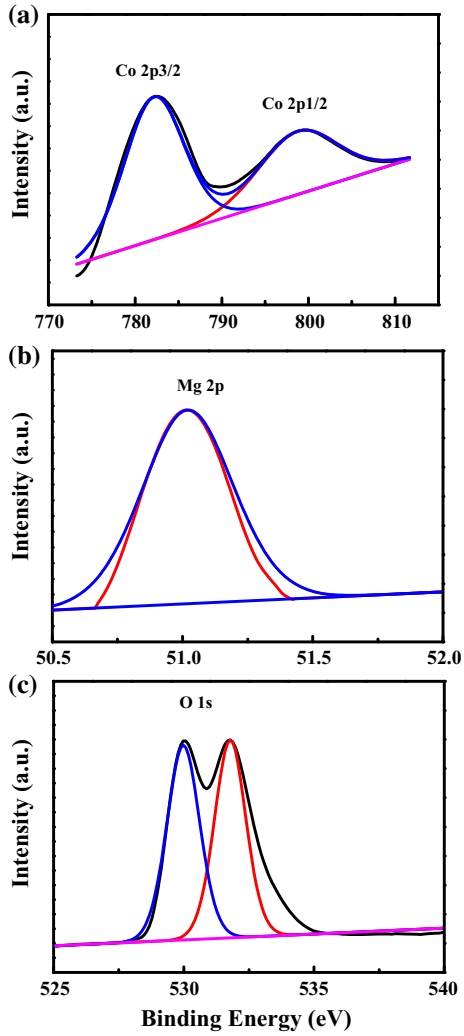

Fig. 3 High-resolution XPS spectra of **a** Co 2p, **b** Mg 2p, and **c** O 1 s for the $MgCo_2O_4$ nanowires peeled down from the Ni foam

the system when no template is used to confine their growth direction (Wang et al. 2013; Cao et al. 2009).

The SEM micrograph, EDS microanalysis, and the corresponding mapping images of the cross-section of $MgCo_2O_4$ nanowires are shown in Fig. 5a–f. The EDS microanalysis of Fig. 5b clearly indicates that the $MgCo_2O_4$ nanowires constitute only Mg, Co, and O elements with atomic ratio of almost of 1:2:4, demonstrating the formation of pure $MgCo_2O_4$ nanowires. The elemental maps shown in Fig. 5c–f provide clearer information about the element spatial distribution within the cross-section of $MgCo_2O_4$

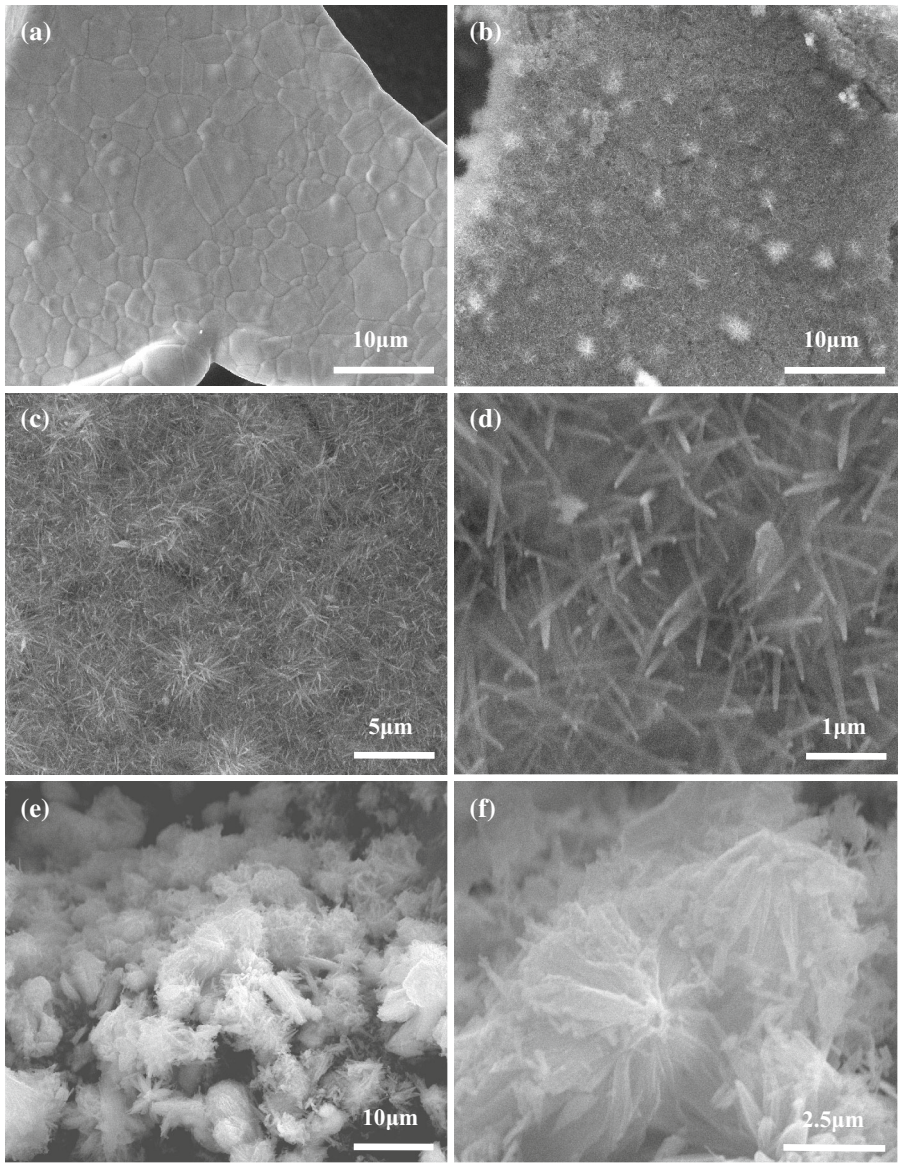

Fig. 4 **a** SEM images of Ni foam, **b–d** SEM photographs of the as-prepared $MgCo_2O_4$ nanowires, **e**, **f** SEM photographs of the as-prepared $MgCo_2O_4$ microspheres

nanowires, which further confirm the formation of pure $MgCo_2O_4$ nanowires products.

To further investigate the detailed morphology and structure of $MgCo_2O_4$ nanowires, TEM, HRTEM, and SAED analysis are employed (Fig. 6a–e). TEM image in Fig. 6a clearly shows that the sample has an edge length of 1–3 μm and a uniform thickness of ~60 nm, which is in good agreement with the SEM observation. HRTEM image in Fig. 6b observation reveals that the porous nanowire consists of quasi-continuous nanoparticles of 10–20 nm in diameter. To analyze the crystal accurately, a HRTEM image is derived from the red rectangle in (Fig. 6c–d). The lattice spacing is measured to be 0.288 nm, in a good agreement with the theoretical interplane spacing of $MgCo_2O_4$ (220) planes. SAED pattern in Fig. 6e implies that these particles are single crystalline in nature. Figure 6f shows a typical TEM image of the $MgCo_2O_4$ microspheres, and it can be clearly seen that each microsphere is composed of many aggregated

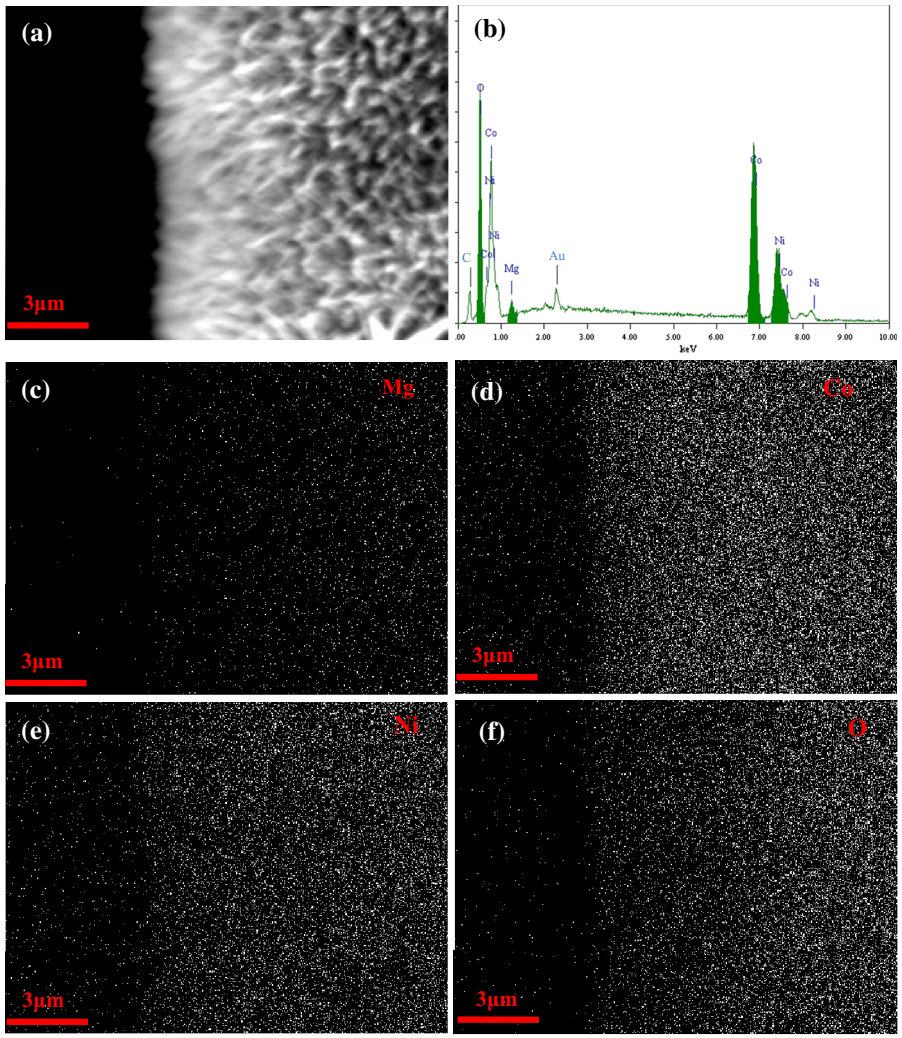

Fig. 5 **a** SEM image and **b** EDS spectrum of $MgCo_2O_4$ nanowire, **c–f** corresponding elemental mappings of Mg, Co, Ni, and O for the $MgCo_2O_4$ nanowire

nanowires. Such a phenomenon is consistent with the SEM image (Fig. 4f).

Figure 7 shows the N_2 adsorption–desorption isotherms and the corresponding BJH pore size distribution plot of $MgCo_2O_4$ nanowires and microspheres. All of the isotherms in Fig. 7a, b can be classified as type IV isotherm with a type-H_4 hysteresis loop, implying the existence of mesoporous structure in the material (Vinu et al. 2005). According to the investigative results, the BET surface areas of $MgCo_2O_4$ nanowires and microspheres are 45.1 and 30.6 $m^2\ g^{-1}$, respectively. According to the corresponding BJH pore size distribution (the inset of Fig. 7) recorded from nitrogen isotherms, the adsorption average pore size is 11.5 nm for $MgCo_2O_4$ nanowires and 9.2 nm for $MgCo_2O_4$ microspheres, which further confirmed the mesoporous feature of these materials. The relatively large specific surface area and identified porosity are beneficial for the Li^+ diffusion and electrode–electrolyte contacts during the electrochemical process.

The electrochemical properties of $MgCo_2O_4$ nanowires as a conductivity-agent-free and binder-free anode for LIBs are examined by CV and discharging and charging test. The initial three CV curves of the electrode between 0 and 3 V (vs. Li/Li^+) at a scan rate

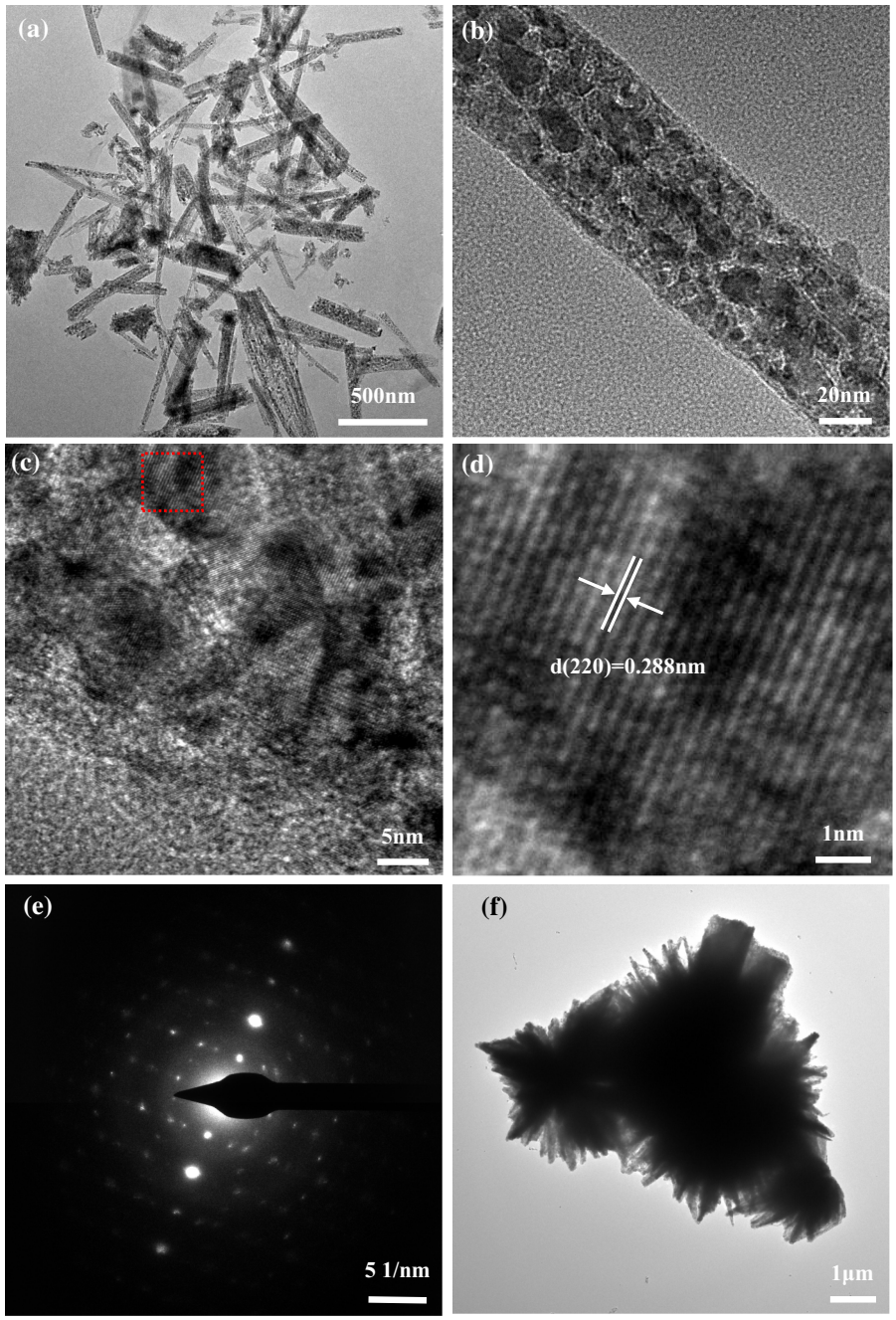

Fig. 6 **a** TEM image of $MgCo_2O_4$ nanowires, **b** TEM image of a $MgCo_2O_4$ nanowire, **c**, **d** HRTE images, **e** SAED pattern of the as-prepared $MgCo_2O_4$ nanowires and **f** TEM image of $MgCo_2O_4$ microspheres

of 0.1 mV s^{-1} are shown in Fig. 8a. It can be seen from the CV results in Fig. 8a that there is a substantial difference between the first and subsequent cycles. The peak at 0.33 V observed in the first discharge CVs is ascribed to the formation of the SEI layer (Eq. (1)) and the reduction of Co^{3+} to metallic Co, Mg^{2+} is not reduced to Mg^0 due to the high bond energy of MgO (Eq. (2)) (Connor and Irvine 2001). At the second scan, the reduction peak shifts to about 0.8 V and becomes broader compared to the first cycle, while the anodic scans almost without changes. Two oxidation peaks are found at 1.6 and 2.3 V. The weak peak at 1.6 V should correspond to the dissolution of the SEI layer, and the strong peak at 2.3 V can be assigned to

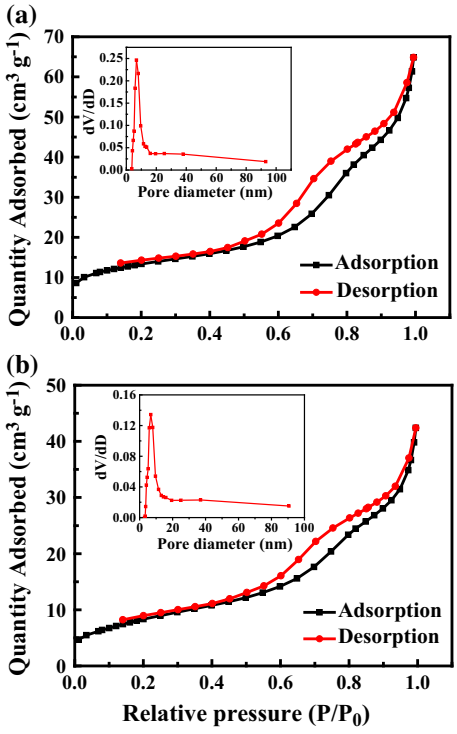

Fig. 7 Nitrogen adsorption/desorption isotherm of **a** $MgCo_2O_4$ nanowires and **b** $MgCo_2O_4$ microspheres, *insets* the corresponding BJH pore size distribution curves calculated from desorption branch

the reaction (Eqs. (3), (4)). Moreover, it is obvious that the peak intensity drops significantly in the second cycle, indicating the occurrence of some irreversible reactions associated with the SEI formation.

$$Li^+ + e^- + \text{electrolyte} \rightarrow \text{SEI}\ (Li) \quad (1)$$

$$MgCo_2O_4 + 6Li^+ + 6e^- \rightarrow 2Co + 2Li_2O + MgO \quad (2)$$

$$2Co + 2Li_2O \leftrightarrow 2CoO + 4Li^+ + 4e^- \quad (3)$$

$$2CoO + 2/3Li_2O \leftrightarrow 2/3Co_3O_4 + 4/3Li^+ + 4/3e^- \quad (4)$$

Figure 8b shows the discharge and charge curves of $MgCo_2O_4$ nanowires electrode for the 1st and 2nd at a current density of 2.5 A g^{-1}. The first discharge and charge capacity are 1357 and 1029 mAh g^{-1}, respectively. Accordingly, the coulombic efficiency of $MgCo_2O_4$ in the first cycle can be calculated to be 76 %. These values are higher than the theoretical capacity of $MgCo_2O_4$. The extra capacity can be ascribed to solid-electrolyte interphase (SEI) formation and the decomposition of electrolytes. Upon the second discharge–charge process, the discharge and charge capacities are 998 and 949 mAh g^{-1},

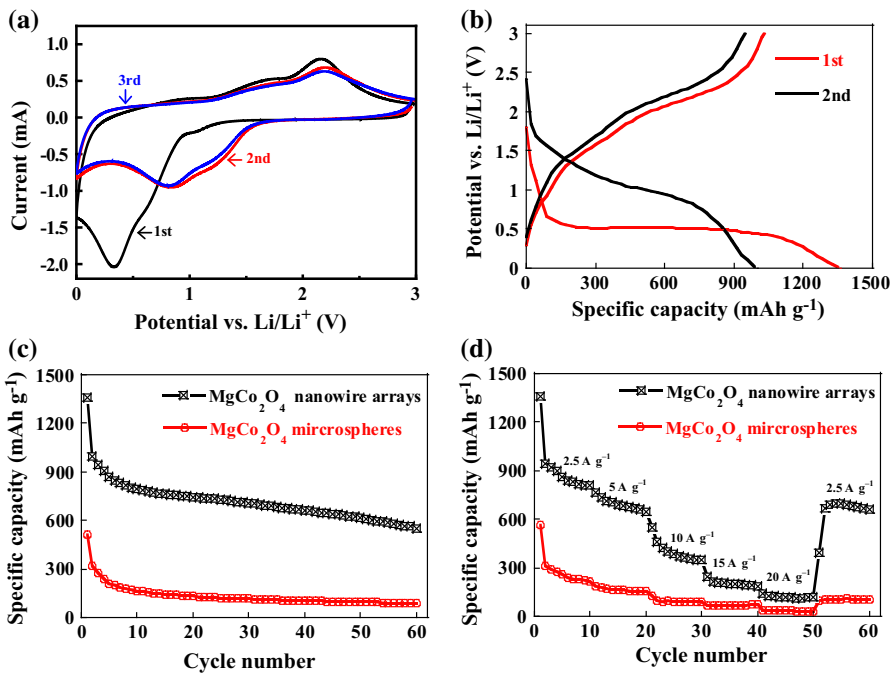

Fig. 8 **a** The first three consecutive CV curves of $MgCo_2O_4$ nanowires at a scan rate of 0.1 mV s^{-1}, **b** the first and second discharge–charge curves at a current density of 2.5 A g^{-1}, and **c** cycle performance of $MgCo_2O_4$ nanowires and microsphere electrode microspheres at a current density of 2.5 A g^{-1}, **d** rate performance of $MgCo_2O_4$ nanowires and microsphere at various current densities

Table 1 Lithium storage performance comparison of $MgCo_2O_4$ nanowires electrodes with previously reported Co-based binary metal oxides

Binary metal oxide	Capacity at low current density	Capacity at high current density	Ref.
$MgCo_2O_4$ nanowire	~940 mAh g^{-1} at 2.5 A g^{-1}	~550 mAh g^{-1} at 10 A g^{-1}	This work
$NiCo_2O_4$ nanoflake	~880 mAh g^{-1} at 0.5 A g^{-1}	~540 mAh g^{-1} at 2 A g^{-1}	Zheng et al. (2015)
$MnCo_2O_4$ microspheres	~940 mAh g^{-1} at 0.2 A g^{-1}	~400 mAh g^{-1} at 2.7 A g^{-1}	Fu et al. (2014)
Ellipsoidal $MnCo_2O_4$	~950 mAh g^{-1} at 0.1 A g^{-1}	~820 mAh g^{-1} at 0.4 A g^{-1}	Huang et al. (2014)
$NiCo_2O_4$ microspheres	~550 mAh g^{-1} at 0.8 A g^{-1}	~390 mAh g^{-1} at 1.6 A g^{-1}	Li et al. (2013)
$ZnCo_2O_4$ microspheres	~970 mAh g^{-1} at 0.1 A g^{-1}	~400 mAh g^{-1} at 5 A g^{-1}	Hu et al. (2013)
$ZnCo_2O_4$ nanowires	~1020 mAh g^{-1} at 0.2 A g^{-1}	~340 mAh g^{-1} at 0.8 A g^{-1}	Mohamed et al. (2013)
$ZnCo_2O_4$ flower-like	~1200 mAh g^{-1} at 0.1 A g^{-1}	~880 mAh g^{-1} at 1 A g^{-1}	Chen et al. (2015)
Nano-phase-$CuCo_2O_4$	~820 mAh g^{-1} at 0.1 A g^{-1}	~380 mAh g^{-1} at 0.752 A g^{-1}	Sharma et al. (2007b)
$FeCo_2O_4$ nanoflakes	~1570 mAh g^{-1} at 0.2 A g^{-1}	~1220 mAh g^{-1} at 0.8 A g^{-1}	Mohamed et al. (2014)
$ZnCo_2O_4$ nanostructure	~1015 mAh g^{-1} at 0.5 A g^{-1}	~606 mAh g^{-1} at 1 A g^{-1}	Song et al. (2014)
Porous $ZnCo_2O_4$	~1550 mAh g^{-1} at 0.1 A g^{-1}	~500 mAh g^{-1} at 5 A g^{-1}	Hao et al. (2015)
Flower-like $MnCo_2O_4$	~330 mAh g^{-1} at 0.05 A g^{-1}	~180 mAh g^{-1} at 0.2 A g^{-1}	Wu et al. (2015)
$MnCo_2O_4$ nanowire	~820 mAh g^{-1} at 0.2 A g^{-1}	~340 mAh g^{-1} at 1 A g^{-1}	Li et al. (2014b)

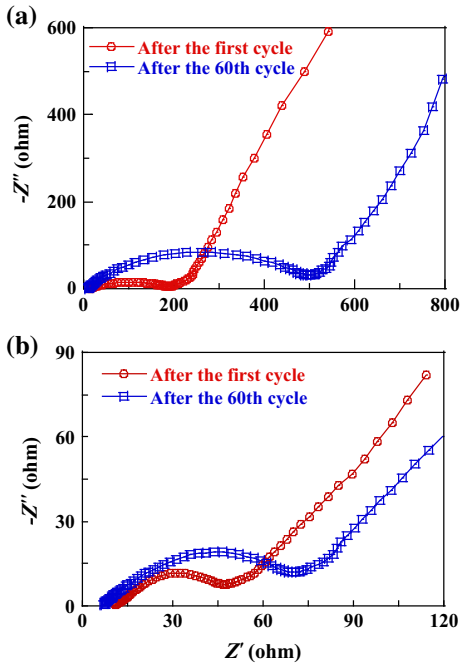

Fig. 9 The Nyquist plots of **a** $MgCo_2O_4$ microsphere and **b** $MgCo_2O_4$ nanowires material after the first cycle and the 60th cycle

respectively; and the coulombic efficiency increases significantly up to about 95 %. Figure 8c gives a comparison of reversible capacity versus cycle number for $MgCo_2O_4$ nanowires and microspheres electrode. As can be seen in Fig. 8c, from the second cycle onwards, the $MgCo_2O_4$ nanowires electrode exhibits slightly capacity decay and around 53 % of the initial reversible capacity can be retained over 60 cycles at a current density of 2.5 A g^{-1}. For $MgCo_2O_4$ microspheres electrode, after 60 cycles, the reversible capacity is only 83 mAh g^{-1}, and the initial reversible capacity is only 22 %. $MgCo_2O_4$ nanowires electrode also shows remarkable rate performance compared to the $MgCo_2O_4$ microspheres electrode. As shown in Fig. 8d, at the current densities increase from 5, 10, 15, and 20 A g^{-1}, and the discharge capacities of the $MgCo_2O_4$ nanowires electrode are about 649, 348, 188, and 121 mAh g^{-1}, respectively. More importantly, when the rate is switched abruptly from 20 to 2.5 A g^{-1}, the specific capacity is exceptionally high at 690 mAh g^{-1}. These results indicate that the $MgCo_2O_4$ nanowires structure has very significant potential for high-rate anode materials in LIBs. While the capacities of $MgCo_2O_4$ microspheres electrode are 155, 88, 75, and 31 mAh g^{-1} at the current densities increase from 5, 10, 15, and 20 A g^{-1}. Apparently, the above results that the improvement in lithium storage properties should attribute to the nanostructured morphology, providing a high-specific surface area to add the contact area between active electrode materials and electrolyte. The high contact area can

also provide more active sites for lithium-ion insertion/extraction. In addition, during the first discharge, Mg metal atoms form inactive MgO, which can inhibit volume variations effectively during the electrochemical reaction. Based on the above discussed electrochemical performance of $MgCo_2O_4$ nanowires electrode, it is found that our produced $MgCo_2O_4$ nanowires exhibited higher rate capability than those of previously reported Co-based binary metal oxides (Table 1).

To explore the cause for the large capacity degradation, EIS of the $MgCo_2O_4$ microsphere and $MgCo_2O_4$ nanowires material after the first cycle and the 60th cycle are shown in Fig. 9. The semicircle stands for the charge-transfer impedance on electrode/electrolyte interface (Cao et al. 2013). It can be seen clearly that the diameter of the semicircle of the $MgCo_2O_4$ nanowire electrode after the first cycle is much smaller than that of the $MgCo_2O_4$ microsphere electrode, demonstrating that the Ni substrate existed in the system increased the charge-transfer process compared to pure powder materials. The results indicate that Ni substrate enhances the conductivity of pure binary metal oxide materials. After the 60th cycles, it is worth noting that the charge-transfer resistance is enlarged for two samples. The increase in charge-transfer resistance can give rise to capacity decay during the cycling process.

Conclusion

In summary, we demonstrated a simple hydrothermal reaction for the synthesis of $MgCo_2O_4$ nanowires at a low temperature as 100 °C. $MgCo_2O_4$ nanowires, assembled by plenty of quasi-continuous nanoparticles, give rise to a BET surface area of 45.1 $m^2\ g^{-1}$ and the adsorption average pore size of 11.5 nm. When tested as an anode for LIBs, the $MgCo_2O_4$ nanowires electrodes exhibit exceptional properties in terms of specific capacity, cycling performance, and rate capacity compared with previously reported Co-based binary metal oxides. The discharge capacities of the $MgCo_2O_4$ nanowires electrode are about 649, 348, 188, and 121 mAh g^{-1}, when the current densities increase from 5, 10, 15, and 20 A g^{-1}, respectively. EIS measurements have confirmed that Ni substrate enhances the conductivity of pure binary metal oxide materials. In addition, $MgCo_2O_4$ nanowires with nanostructure can provide numerous efficient transport pathways for ions and electrons and relieve the pulverization of active anode material during charging/discharging processes.

Acknowledgments This work was supported by the financial supports of the National Natural Science Foundation of China (Nos. 21301140 and 21061130551), and the Natural Science Foundation of Shaanxi Province (No. 2013JQ2004).

References

Aravindan V, Kumar PS, Sundaramurthy J, Ling WC, Ramakrishna S, Madhavi S (2013) Electrospun NiO nanofibers as high performance anode material for Li-ion batteries. J Power Sources 227:284–290

Bai J, Li XG, Liu GZ, Qian YT, Xiong SL (2014) Unusual formation of $ZnCo_2O_4$ 3D hierarchical twin microspheres as a high-rate and ultralong-life lithium-ion battery anode material. Adv Funct Mater 24:3012–3020

Cao F, Hu W, Zhou L, Shi W, Song S, Lei Y, Wang S, Zhang H (2009) 3D Fe_3S_4 flower-like microspheres: high-yield synthesis via a biomolecule-assisted solution approach, their electrical, magnetic and electrochemical hydrogen storage properties. Dalton Trans 42:9246–9252

Cao F, Pan GX, Tang PS, Chen HF (2013) NiO nanowall array prepared by a hydrothermal synthesis method and its enhanced electrochemical performance for lithium ion batteries. Mater Res Bull 48:1178–1183

Casey P, Hughes G, O'Connor E, Long RD, Hurley PK (2008) Growth and characterisation of thin MgO layers on Si(100) surfaces. J Phys: Conf Ser 100:42–46

Chamas M, Sougrati MT, Reibel C, Lippens PE (2013) Quantitative analysis of the initial restructuring step of nanostructured $FeSn_2$-based anodes for Li-ion batteries. Chem Mater 25:2410–2420

Chen HW, Liu AF, Zhang XL, Mu JB, Bai YM, Hou JX (2015) Three-dimensional hierarchical $ZnCo_2O_4$ flower-like microspheres assembled from porous nanosheets: hydrothermal synthesis and electrochemical properties. Ceram Int 41:7556–7564

Cherian CT, Sundaramurthy J, Reddy MV, Kumar PS, Mani K, Pliszka D, Sow CH, Ramakrishna S, Chowdari BVR (2013) Morphologically robust $NiFe_2O_4$ nanofibers as high capacity Li-ion battery anode material. ACS Appl Mater Interfaces 5:9957–9963

Connor PA, Irvine JTS (2001) Novel tin oxide spinel-based anodes for Li-ion batteries. J Power Sources 223:97–98

Corneille JS, He JW, Goodman DW (1994) XPS characterization of ultra-thin MgO films on a Mo (100) surface. Surf Sci 306:269–278

Du N, Xu YF, Zhang H, Yu JX, Zhai CX, Yang D (2011) Porous $ZnCo_2O_4$ nanowires synthesis via sacrificial templates: high-performance anode materials of Li-ion batteries. Inorg Chem 50:3320–3324

Fu YJ, Yang ZB, Li XW, Wang XH, Liu DQ, Hu DK, Qiao L, He DY (2013) Template-free synthesized Ni nanofoams as

nanostructured current collectors for high-performance electrodes in lithium ion batteries. J Mater Chem A 1:10002–10007

Fu CC, Li GS, Luo D, Huang XS, Zheng J, Li LP (2014) One-step calcination-free synthesis of multicomponent spinel assembled microspheres for high-performance anodes of Li-ion batteries: a case study of $MnCo_2O_4$. ACS Appl Mater Interfaces 6:2439–2449

Hao SJ, Zhang B, Ball S, Copley M, Xu ZC, Srinivasan M, Zhou K, Mhaisalkar S, Huang YZ (2015) Synthesis of multi-modal porous $ZnCo_2O_4$ and its electrochemical properties as an anode material for lithium ion batteries. J Power Sources 294:112–119

Hu LL, Qu BH, Li CC, Chen YJ, Mei L, Lei DN, Chen LB, Li QH, Wang TH (2013) Facile synthesis of uniform mesoporous $ZnCo_2O_4$ microspheres as a high-performance anode material for Li-ion batteries. J Mater Chem A 1:5596–5602

Huang GY, Xu SM, Xu ZH, Sun HY, Li LY (2014) Core-shell ellipsoidal $MnCo_2O_4$ anode with micro-/nano-structure and concentration gradient for lithium-ion batteries. ACS Appl Mater Interfaces 6:21325–21334

Kang WP, Feng F, Zhang MM, Liu SJ, Shen Q (2013) Structural features and electrochemical properties of nanostructured $ZnCo_2O_4$ synthesized by an oxalate precursor method. J Nanopart Res 15:1891–1897

Li LM, Yin XM, Liu S, Wang YG, Chen LB, Wang TH (2010) Electrospun porous SnO_2 nanotubes as high capacity anode materials for lithium ion batteries. Electrochem Commun 12:1383–1386

Li JF, Xiong SL, Liu YR, Ju ZC, Qian YT (2013) High electrochemical performance of monodisperse $NiCo_2O_4$ mesoporous microspheres as an anode material for Li-ion batteries. ACS Appl Mater Interfaces 5:981–988

Li JF, Wang JZ, Liang X, Zhang ZJ, Liu HK, Qian YT, Xiong SL (2014a) Hollow $MnCo_2O_4$ submicrospheres with multi-level interiors: from mesoporous spheres to yolk-in-double-shell structures. ACS Appl Mater Interfaces 6:24–30

Li L, Zhang YQ, Liu XY, Shi SJ, Zhao XY, Zhang H, Ge X, Cai GF, Gu CD, Wang XL, Tu JP (2014b) One-dimension $MnCo_2O_4$ nanowire arrays for electrochemical energy storage. Electrochim Acta 116:467–474

Liu CJ, Xue FH, Huang H, Yu XH, Xie CJ, Shi MS, Cao GZ, Jung YG, Dong XL (2014) Preparation and electrochemical properties of Fe–Sn (C) nanocomposites as anode for lithium-ion batteries. Electrochim Acta 129:93–99

Lou FL, Zhou HT, Tran Buan MEM, Bruer FV, Rønning M, Walmsley JC, Chen D (2014) Coaxial carbon/metal oxide/aligned carbon nanotube arrays as high-performance anodes for lithium ion batteries. ChemSusChem 7:1335–1346

Luo W, Hu XL, Sun YM, Huang YH (2012) Electrospun porous $ZnCo_2O_4$ nanotubes as a high-performance anode material for lithium-ion batteries. J Mater Chem 22:8916–8921

Mohamed SG, Hung TF, Chen CJ, Chen CK, Hu SF, Liu RS, Wang KC, Xing XK, Liu HM, Liu AS, Hsieh MH, Lee BJ (2013) Flower-like $ZnCo_2O_4$ nanowires: toward a high performance anode material for Li-ion batteries. RSC Adv 3:20143–20149

Mohamed SG, Chen CJ, Chen CK, Hu SF, Liu RS (2014) High-performance lithium-ion battery and symmetric supercapacitors based on $FeCo_2O_4$ nanoflakes electrodes. ACS Appl Mater Interfaces 6:22701–22708

Mondal AK, Su D, Chen SQ, Xie XQ, Wang GX (2014) Highly porous $NiCo_2O_4$ nanoflakes and nanobelts as anode materials for lithium-ion batteries with excellent rate capability. ACS Appl Mater Interfaces 6:14827–14835

Sharma BY, Sharma N, Rao GVS, Chowdari BVR (2007a) Nanophase $ZnCo_2O_4$ as a high performance anode material for Li-ion batteries. Adv Funct Mater 17:2855–2861

Sharma Y, Sharma N, Rao GVS, Chowdari BVR (2007b) Lithium recycling behaviour of nano-phase-$CuCo_2O_4$ as anode for lithium-ion batteries. J Power Sources 173:495–501

Sharma Y, Sharma N, Rao GVS, Chowdari BVR (2008) Studies on spinel cobaltites, $FeCo_2O_4$ and $MgCo_2O_4$ as anodes for Li-ion batteries. Solid State Ionics 179:587–597

Shen LF, Che Q, Li HS, Zhang XG (2014) Mesoporous $NiCo_2O_4$ nanowire arrays grown on carbon textiles as binder-free flexible electrodes for energy storage. Adv Funct Mater 24:2630–2637

Song X, Ru Q, Mo YD, Hu SJ, An B (2014) A novel fiber bundle structure $ZnCo_2O_4$ as a high capacity anode material for lithium-ion battery. J Alloy Compd 60:6219–6225

Tian B, Zheng XT, Kempa J, Fang Y, Yu N, Yu G, Huang J, Lieber CM (2007) Coaxial silicon nanowires as solar cells and nanoelectronic power sources. Nature 449:885–889

Vinu A, Sawant DP, Ariga K, Hartmann M, Halligudi SB (2005) Benzylation of benzene and other aromatics by benzyl chloride over mesoporous AlSBA-15 catalysts. Microporous Mesoporous Mater 80:195–203

Wang XH, Li XW, Sun XL, Li F, Liu QM, Wang Q, He DY (2011) Nanostructured NiO electrode for high rate Li-ion batteries. J Mater Chem 21:3571–3573

Wang G, Wang H, Bai J, Ren Z (2013) PVP-assisted assembly of lanthanum carbonate hydroxide with hierarchical architectures and their luminescence properties. Chem Eng J 214:386–393

Wu XH, Wu WW, Wang KT, Chen W, He D (2015) Synthesis and electrochemical performance of Wu-like $MnCo_2O_4$ as an anode material for sodium ion batteries. Mater Lett 147:85–87

Xiao YL, Zai JT, Tao LQ, Li B, Han QY, Yu C, Qian XF (2013) $MnFe_2O_4$–graphene nanocomposites with enhanced performances as anode materials for Li-ion batteries. Phys Chem Chem Phys 15:3939–3945

Xie QS, Li F, Guo HZ, Wang LS, Chen YZ, Yue GH, Peng DL (2013) Template-free synthesis of amorphous double-shelled zinc-cobalt citrate hollow microspheres and their transformation to crystalline $ZnCo_2O_4$ microspheres. ACS Appl Mater Interfaces 5:5508–5517

Yuan CZ, Li JY, Hou LR, Zhang XG, Shen LF, Lou XW (2012) Ultrathin mesoporous $NiCo_2O_4$ nanosheets supported on Ni foam as advanced electrodes for supercapacitors. Adv Funct Mater 22:4592–4597

Zhao XY, Cao MH, Hu CW (2012) Binder strategy towards improving the rate performance of nanosheet assembled SnO_2 hollow microspheres. RSC Adv 2:11737–11742

Zheng QY, Zhang XY, Shen YM (2015) Fabrication of free-standing $NiCo_2O_4$ nanoarrays via a facile modified hydrothermal synthesis method and their applications for lithium ion batteries and high-rate alkaline batteries. Mater Res Bull 63:211–215